

An In Situ Resistance-Based Method for Tracking the Temporal Evolution of Recovery and Recrystallization in Ni-Base Single-Crystal Superalloy at Super-Solvus Temperatures



S.J. PERRY, N. D'SOUZA, D.M. COLLINS, B. ROEBUCK, and H.B. DONG

This study explores the influence of thermo-mechanical behavior and microstructure on recovery and recrystallization in single-crystal superalloys during casting and subsequent solution heat treatment, using miniature testing. Here, the temporal evolution of resistance was measured using *in situ* electrothermal mechanical testing (ETMT) to track the process of recovery and recrystallization (RX). It was found that recrystallization is dominant only when recovery is incomplete and is dependent on both the history dependence of the strain path as well as the magnitude of the accumulated plastic strain. A precursor to recrystallization is the occurrence of subgrains and deformation twins on the sample surface, where a characteristic butterfly-type morphology of γ' precipitates is always observed in highly strained regions. The migration of RX grain boundaries is accompanied by the elimination of lattice curvature associated with the density of geometrically necessary dislocations. Homogenized samples provide the most reliable results, while interpreting resistivity changes with recovery and recrystallization is more challenging when inhomogeneity (microsegregation, local variation of mechanical properties) in as-cast material prevails.

<https://doi.org/10.1007/s11661-022-06861-5>
© The Author(s) 2022

I. INTRODUCTION

NI-BASE alloys are widely used for high-temperature applications, such as the turbine module of the jet engine. These alloys possess a unique combination of high temperature strength, ductility, toughness, and good oxidation properties, making them the alloy of choice for the manufacture of turbine blades. Their superior mechanical performance is derived from a microstructure comprising an Al disordered γ matrix and a fine dispersion of ordered, L1₂ ordered γ' precipitates. Further, rotating components, such as turbine blades requiring high-temperature creep resistance and ductility, are manufactured in single-crystal form using the state-of-the-art directional solidification process.^[1,2] While turbine blade components manufactured from Ni-base superalloys have exceptional

strength at elevated operating temperatures, they are vulnerable to undesirable plastic deformation following casting and heat treatment, specifically around the γ' solvus temperature ~ 1260 °C.^[3] With increasing turbine entry temperatures (TET), the design of complex internal air-cooling passages has led to very complicated blade designs. During casting and subsequent homogenization of the extensively segregated as-cast microstructure, internal stress concentration features arising within complex cooling passage pose potent sites for recrystallization leading to rejection of the component.^[4]

Deformed microstructures undergo two key stages by which the material reduces the internally stored energy following deformation: recovery and recrystallization. During recovery, dislocations re-arrange themselves into low energy configurations, such as polygonization. Recrystallization requires subgrain migration to form a high-angle boundary with high mobility leading to rapid annihilation of dislocations as this boundary sweeps through the strained matrix.^[5] This occurs dynamically at high strain rates during thermo-mechanical deformation, such as in forging. Alternatively, static recrystallization is seen at lower strain rates during subsequent heat treatment, as in directional solidification. It has been shown that recovery is a precursor to recrystallization and that the rearrangement of the

S.J. PERRY and H.B. DONG are with the University of Leicester, Leicester, LE1 7RH, UK. Contact e-mail: sjp78@leicester.ac.uk. N. D'SOUZA is with the Rolls Royce Plc, Derby, DE24 8BJ, UK. D.M. COLLINS is with the University of Birmingham, Birmingham, B15 2TT, UK. B. ROEBUCK is with the National Physical Laboratory, Teddington, TW11 0LW, UK.

Manuscript submitted August 10, 2022; accepted October 14, 2022.

Article published online November 8, 2022

subgrain structure is an important step in the formation of a stable nucleus. However, it is important that a clear distinction is made between the two processes. Recrystallization essentially constitutes the formation of new defect-free grains with high-angle boundaries, which grow in the deformed material.^[6] The formation of such secondary grains with random misorientation within the single-crystal matrix is extremely detrimental to the creep rupture life,^[7] and extensive efforts are made to avoid recrystallization.

There have been many studies devoted to investigating different aspects of recrystallization. The *first approach* pertains to studies into the details of the micro-mechanics of recrystallization, which has focused on the origins of embryos and subsequent evolution of these into a critical nucleus characterized by a high-angle boundary that then sweeps through the strained matrix.^[8,9] The classical origins of embryos are attributed to the existence of regions of intense deformation or subgrains, which originate in regions of heterogeneous deformation within the microstructure. In single crystals, this has been shown to occur at a Bridgman notch during creep of a tensile specimen,^[10] but such type of discontinuities in cross sections also arise owing to the internal cooling passages within the turbine blade. More recently, Mathur^[11] proposed an alternate opinion based on a detailed analysis of the as-cast structure, where it was shown that small high-angle grains exist after casting and with a predilection to the surface. These occur within regions of any surface eutectic^[12] or as regions of intense deformation with misorientations up to ~ 20 deg and within $\sim (5 \text{ to } 20 \mu\text{m})$ from the surface. It is proposed that these high-angle grains then grow into the strained matrix and constitute recrystallized grains during homogenization heat treatment.

The *second approach* is directed at modeling the evolution of plastic strain and stress during casting with an aim to establishing thresholds for recrystallization.^[13–16] Specifically, this was conducted using electrothermal mechanical testing (ETMT) capable of measuring a wide range of mechanical and physical properties.^[17–20] It was proposed that not only was the history dependence of the strain path crucial, but it also pointed to the existence of a critical temperature range to delineate the work hardening portion of the plastic strain from the creep strain; the former being associated with an increasing dislocation density leading to recrystallization.^[17,21] In polycrystalline alloys, improved experimental data have led to the development of crystal plasticity finite element (CPFE) models which are capable of simulating loading and dynamic recrystallization; however, experimental data to validate such models for deformation during directional solidification are sparse, with most studies instead exploring isothermal, cold deformation.^[22,23] If this study can show that subgrain microstructural data can be inferred from the electrical properties, this will create opportunities for similar dislocation density-based CPFE modeling and more accurate simulation of recrystallization from directional solidification.

In both approaches, the detection of recrystallization is always post-mortem. Hence, it is not possible to delineate the occurrence of recovery, which precedes recrystallization and depending on the extent of which, recrystallization can also be suppressed.

In lieu of previous studies, the present paper focuses on the key aspects of recovery and recrystallization. First, following the approach taken in a prior study,^[11] we explore the occurrence of surface grains through displacement-controlled cooling experiments under casting relevant conditions given that the surface grains can be the precursor of recrystallization. Specifically, we begin with specimens extracted *internally* from a test bar, which precludes the initial presence of any cast surface defects. From these samples, their evolution and the accompanying strain accumulation that exists within the matrix following cooling can be characterised. Second, we develop a method for *in situ* tracking recovery/recrystallization through a change in resistance, since the latter is also affected by resistivity.^[24] Motivated by this, we aim to address the following questions:

- (1) Do surface grains form during displacement-controlled cooling akin to casting conditions? What are the effects of local misorientation changes on electrical resistivity?
- (2) What is the role of the prior strain path on recovery and recrystallization? Further, can this be accomplished by comparing the effect of isothermal strain, and the strain accumulated during displacement-controlled cooling, akin to casting conditions?
- (3) Can the progression of recovery and recrystallization be captured by the temporal change in resistance during an isothermal hold simulated in the ETMT?

II. MATERIALS AND EXPERIMENTAL METHODOLOGY

A. Materials

Tests here were conducted on the single-crystal Ni-base superalloy, CMSX-4 alloy, with composition given in Table I. Cast bars, of length ~ 60 mm and diameter ~ 10 mm, were machined into matchstick test specimens of dimensions $40 \text{ mm} \times 2 \text{ mm} \times 1 \text{ mm}$ using an electro-discharge machine (EDM). The re-cast layer and any machining-related surface residual stresses were removed with fine diamond abrasive media following grinding of the surfaces. Solutioned specimens were obtained from homogenized bars manufactured under the same directional solidification procedure before subjecting samples to a solutioning heat treatment. The solutioning temperature was $1312 \text{ }^\circ\text{C}$ with an isothermal hold of 6 hours prior to rapid cooling and subsequent primary aging at $1140 \text{ }^\circ\text{C}$ for 2 hours.

B. Electrothermal Mechanical Testing (ETMT)

Electrothermal mechanical testing (ETMT) is a technique developed at the National Physical Laboratory (NPL) capable of measuring a wide range of mechanical and physical properties in miniature test specimens.^[17–20] The ETMT equipment used for these experiments is fitted with a ± 0.5 kN load cell and provides resistance heating to test specimens *via* direct current (DC) across the specimen. Temperature is controlled *via* a Type-R Pt/Pt-13 pct Rh thermocouple spot welded along the center of the gage length \sim (2.75 to 3 mm) where the temperature is uniform within ± 1 K.^[17] Resistance changes are measured between two Pt/Pt-13 pct Rh wires attached within the isothermal gage length of the specimen. All specimens were displaced in the same crystallographic direction [001], *i.e.*, along the length of the test piece.

Continuous cooling experiments under conditions representative of directional solidification akin to^[17] were carried out with details given in Table II using both as-cast and solutioned pedigrees. Unless specified, heating and cooling were set at $1\text{ }^{\circ}\text{C s}^{-1}$ above $800\text{ }^{\circ}\text{C}$. Samples S1, S2, S4, and S5 were further subjected to an isothermal hold to quantify the extent of recovery and recrystallization. All experiments were performed under inert conditions using Ar + 5 pct H₂.

Table I. Nominal Composition of CMSX-4 Ni-Based Superalloy

Element	Ni	Cr	Co	Al	Ti	Ta	W	Mo	Hf	Re
Wt pct	bal	6.5	9.6	5.6	1.0	6.5	6.4	0.6	0.1	3.0

Table II. Experimental Parameters Used for Samples S1–S5 During ETMT

	Stage I	Stage II	Stage III
S1 As-cast specimen, Continuous cooling and isothermal hold	25 °C–1300 °C–1150 °C–1300 °C zero load	1300 °C–1140 °C continuous cooling $\Delta T/\Delta t = -0.1\text{ }^{\circ}\text{C s}^{-1}$ $\dot{\epsilon} = 0.08\text{ }\mu\text{m s}^{-1}$	1290 °C isothermal hold Zero load, 4-hours
S2 Solutioned specimen, Continuous cooling and isothermal hold	25 °C–1300 °C–1150 °C–1300 °C zero Load	1300 °C–1140 °C continuous cooling $\Delta T/\Delta t = -0.1\text{ }^{\circ}\text{C s}^{-1}$ $\dot{\epsilon} = 0.08\text{ }\mu\text{m s}^{-1}$	1290 °C isothermal hold zero load, 4-hours
S3 Notched solutioned specimen, Continuous cooling	25 °C–1300 °C–1150 °C–1300 °C zero load	1300 °C–1210 °C continuous cooling $\Delta T/\Delta t = -0.1\text{ }^{\circ}\text{C s}^{-1}$ $\dot{\epsilon} = 0.08\text{ }\mu\text{m s}^{-1}$	none
S4 Solutioned specimen, Isothermal hold	25 °C–1300 °C–1150 °C zero load	1150 °C isothermal hold $\dot{\epsilon} = 0.04\text{ }\mu\text{m s}^{-1}$	1280 °C isothermal hold zero load, 4-hours
S5 Solutioned specimen, Isothermal hold	25 °C–1300 °C–1150 °C zero load	1150 °C isothermal hold $\dot{\epsilon} = 0.08\text{ }\mu\text{m s}^{-1}$	1280 °C isothermal hold Zero load, 4-hours

1. Experiment 1: Continuous Cooling (Samples S1, S2, and S3)

The material was subjected to a cyclic heating regime seen in Figure 1. The initial resistivity profile of the material was measured under zero-load cooling from room temperature to $1300\text{ }^{\circ}\text{C}$ then dropping to $1150\text{ }^{\circ}\text{C}$ shown as *Stage I*. This strategy provided a baseline resistance profile. Subsequently in *Stage II*, the specimen was reheated to $1300\text{ }^{\circ}\text{C}$ and displacement-controlled cooling [enlarged in Figure 1(b)] was performed from 1300 to $1140\text{ }^{\circ}\text{C}$, giving rise to plastic strain accumulation during this phase. The plastic strain was calculated from continual resistance measurements obtained during the experiment. Before *Stage III*, the sample S1 was heated from room temperature to $1000\text{ }^{\circ}\text{C}$ and subjected to isothermal oxidation to minimize sublimation during the subsequent solutioning cycle owing to the presence of a surface oxide. Following oxidation, the sample was cooled to room temperature at $0.5\text{ }^{\circ}\text{C s}^{-1}$ where the chamber was purged with Ar + 5 pct H₂. In *Stage III*, the sample was heated up to $1290\text{ }^{\circ}\text{C}$ at $1\text{ }^{\circ}\text{C s}^{-1}$ where the specimen was held for 4 hours. Sample S2 was subjected to the same cycle but without oxidation. Sample S3 was subjected to a different cycle, with no oxidation or annealing and displacement-controlled cooling ceased at $1210\text{ }^{\circ}\text{C}$.

2. Experiment 2: Isothermal Displacement (Samples S4 and S5)

Figure 2 displays the cyclic heating profile used in the isothermal displacement experiments. *Stage I* of the isothermally displaced experiments was equivalent to that seen in Figure 1. In *Stage II*, the specimens were cooled under zero load to $1150\text{ }^{\circ}\text{C}$ where they

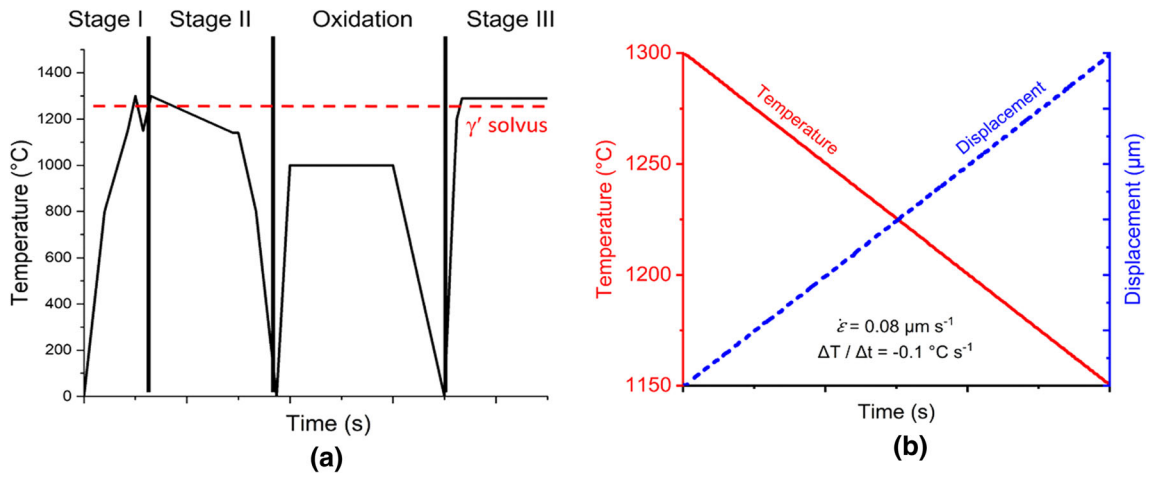


Fig. 1—(a) Thermal profile defined for ETMT testing with displacement-controlled cooling for samples S1, S2 and S3, and (b) the applied displacement and cooling rates during *Stage II*.

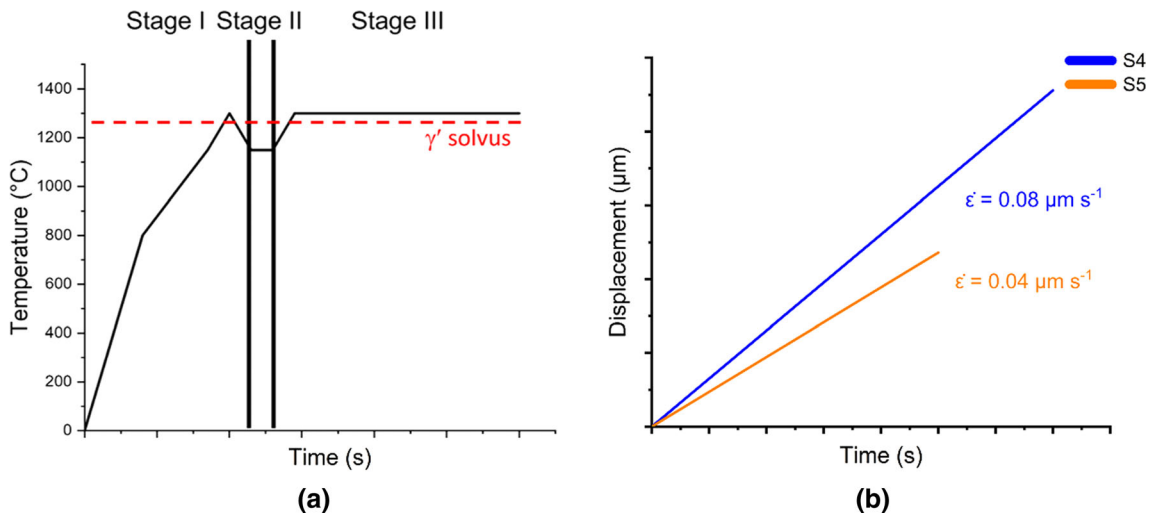


Fig. 2—(a) Thermal profile defined for ETMT in isothermal experiments, and (b) the applied displacement rates during the 1150 °C isothermal hold.

underwent isothermal displacement to induce varying levels of plastic strain. No oxidation was required for the solutioned specimens as other trials outside this work had shown that solutioned specimens were less vulnerable to sublimation during prolonged holds at high temperature. In *Stage III*, the specimens were heated to 1280 °C at 1 °C s⁻¹ where they were held for 4 hours.

C. Plastic Strain Measurement

The plastic strain, ϵ_{pl} , is calculated from resistance measurements using Eq. [1], as shown in.^[17]

$$\epsilon_{pl} = \frac{1}{2} \ln \left(\frac{R_1}{R_0} \right), \quad [1]$$

where R_0 is the resistance within the initially measured, unloaded sample gage and R_1 is the resistance within the strained sample gage. Since the plastic strain

is measured from the resistance, any error in the resistance measurement contributes to an error in the plastic strain. The current and voltage measurements are made with better than 1 part in 10⁴ uncertainty and the maximum range in the measured resistance is ± 0.002 m Ω and with an accompanying standard deviation of ± 0.001 m Ω . A plastic strain resolution of ~ 0.05 pct is estimated from the error in resistance.

The evolution of resistance over the period of the isothermal holds as well as the grip displacement is measured to account for any creep during isothermal holding. On completion of the hold, the sample is cooled under zero load to RT at 10 °C s⁻¹.

D. Electron Microscopy

A combination of backscattered electron imaging (BSE) and electron backscattered diffraction (EBSD) were used to study the post-mortem microstructure. Specimens were mounted in conductive resin before being

ground and polished to 0.05 μm colloidal silica. BSE imaging was performed using a Quanta 4000 FEG-SEM with an acceleration voltage of 20 kV at a working distance of 10 mm. EBSD was performed using a JEOL 7200F equipped with an X-Act EBSD detector operating at 20 kV acceleration voltage and with an emission current of 71.6 μA at a working distance of 15 mm. The pattern resolution was set to 1240×1024 pixels² per image with step size varying from 0.15 μm for observing the substructure, and 7.5 μm for measurements across the full gage length. The Aztec EBSD software was used for data acquisition, pattern indexing, and montage fitting.

Post-processing of EBSD images was carried out using a combination of packages. Oxford instruments CHANNEL-5 software suite was used for denoising images and grain orientation measurements. The Matlab MTEX package^[25] was used for calculating the geometrically necessary dislocations (GND)^[26] and kernel average misorientation (KAM) using customized Matlab script.

III. RESULTS

A. Evolution of Resistance and Microstructure Following Continuous Cooling and Isothermal Hold

The normalized resistance following^[17] with temperature during the initial zero-load heating cycle is shown in Figure 3. The γ' solvus temperature of sample S2 is evident with a plateau at ~ 1260 °C. In contrast, in the case of the as-cast condition, sample S1, the γ' solvus temperature is smeared owing to the contribution of the eutectic,^[17] which is also enriched in γ' partitioning elements, which is not seen in the case of sample S2, which had been homogenized *via* a solution heat treatment prior to the displacement-controlled cooling.

To address the implications of the evolving plastic strain and stress during continuous cooling, the 2nd cooling run for samples S1, S2, and S3 is considered, where the sample was cooled under displacement-controlled conditions (Table II). Figure 4(a) shows the evolution of stress and plastic strain with temperature while Figure 4(b) plots the evolution of stress and plastic strain. There are two key observations:

- An initial period of easy glide is observed up to ~ 1225 °C, where there is a small increase in stress up to $\sim (10$ to 15 MPa), but a notable increase in plastic strain up to ~ 2 pct.
- A rapid increase in stress is observed below ~ 1225 °C implying that hardening begins to increasingly prevail. This correlates with the temperature at which γ' has nucleated and the yield strength of the material progressively increases, which is consistent with observations in other Ni-base superalloys.^[27]

The homogenized specimen (sample S2) shows similar strengthening behavior to sample S1. The total plastic strain for S3 was lower, owing to the termination of the test at 1215 °C. The evolution of stress follows a similar pattern to sample S1.

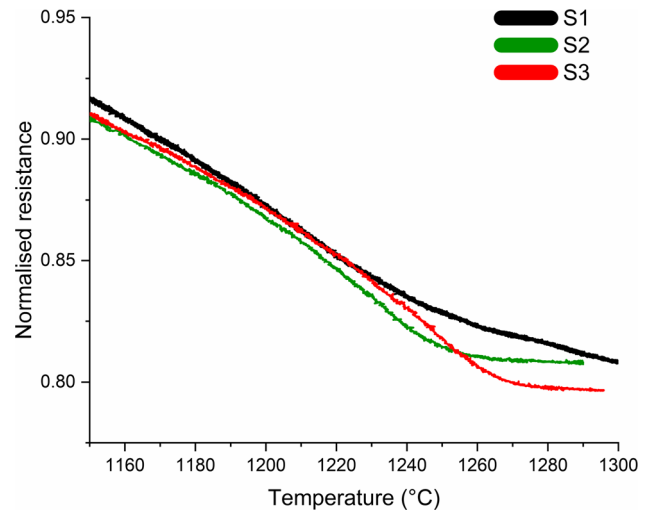


Fig. 3—*Stage I*: Plot of normalized resistance vs temperature during the 1st heating (1 °C s^{-1}) cycle under zero load for samples S1, S2, and S3.

The plastic strain accumulated within the specimen, as in Figures 4(a) and (b), is commonly modeled as the driving force for recrystallization,^[3] with the tacit assumption that it is proportional to the dislocation density. This aspect is now addressed, where samples S1 and S2 are subsequently subjected to an isothermal hold representing a homogenization cycle. Accordingly, in Figures 5(a) and (b), the temporal evolution of normalized resistance, $R(t)$ is presented, where the isothermal hold is carried out under zero load. Values are normalized using the room temperature resistance. The change in grip displacement with time is also shown in Figure 5. Three key observations can be made:

- There is only a small variation in grip displacement observed in each sample. In sample S1, a change in grip displacement of ~ 5 μm occurs over the period of the isothermal hold of ~ 3.5 hours. In sample S2, the change is ~ 3 μm over the same period. Given these values, the creep strain applied during the isothermal hold is assumed to be negligible.
- In sample S1, there is a continual decrease in $R(t)$ which can be divided into 3 regimes; an initial gradual decrease up to ~ 4000 s, a more accelerated decrease up to 8000 s, and a further gradual decrease thereafter.
- In sample S2, there is an initial sharp decrease in $R(t)$ up to 1800s followed by a decelerated gradual decrease thereafter.

For the as-cast condition, there is a concomitant dissolution of the non-equilibrium eutectic through homogenization. Dissolution of the γ' -rich eutectic also leads to a decrease in resistivity since the intrinsic resistivity of γ is less than the γ' phase.^[19] This aspect will be considered in more detail in the discussion. The evolving microstructure in sample S1 also needs to be addressed in relation to the decreasing resistivity. Grain orientation data are shown from EBSD measurements, Figure 6(a), with an inverse pole figure (IPF-Z) with Z

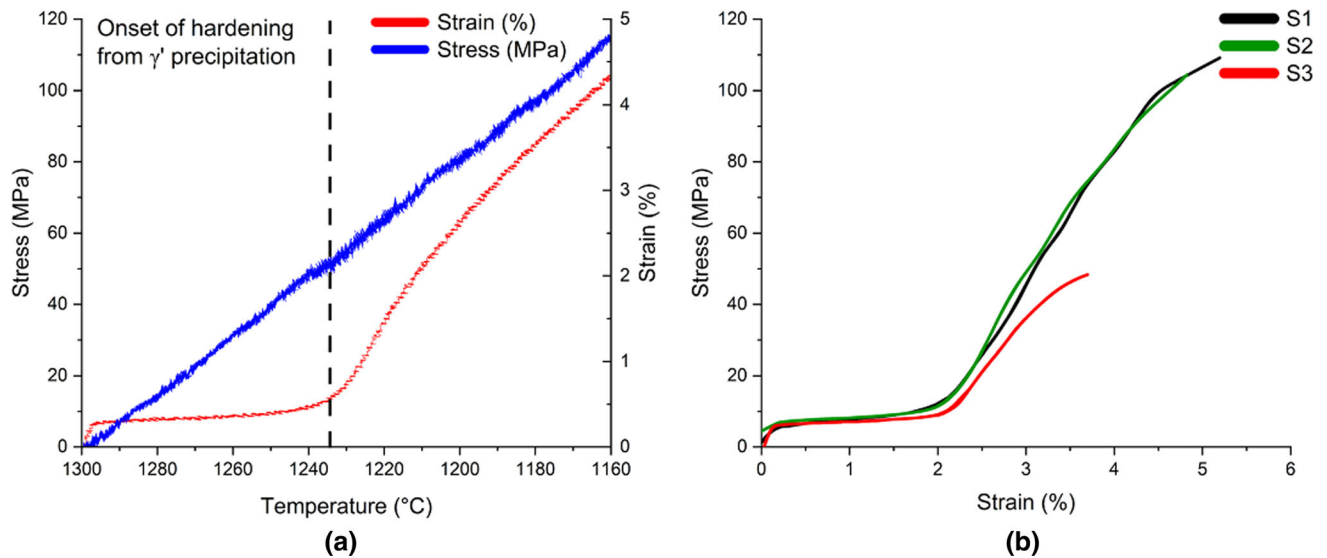


Fig. 4—Stage II: Evolution of stress and plastic strain during displacement-controlled cooling during for sample S1. The onset of work hardening as γ' forms can be seen ~ 1220 °C. (a) Stress and plastic strain with temperature and (b) stress vs plastic strain with the onset of hardening seen at ~ 2.0 pct for samples S1, S2, and S3.

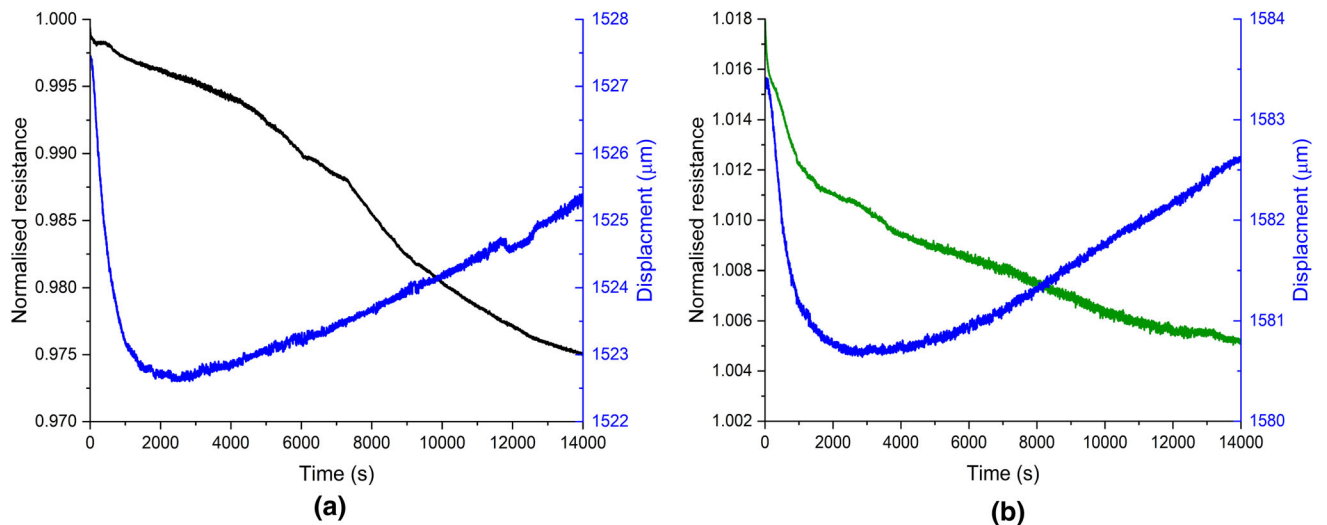


Fig. 5—Stage III: Evolution of normalized resistance and grip displacement with time for (a) sample S1 during an isothermal hold at 1290 °C (b) sample S2 during an isothermal hold at 1290 °C.

being the specimen length, while Figure 6(b) shows a subset region containing surface grains, collected with a higher spatial resolution. Figure 6(c) shows the misorientation between successive measurement points [following the black line in Figure 6(b)]. The following observations can be made:

- The bulk of the gage length does not show any evidence of profuse recrystallized grains, *i.e.*, grains with random orientations. However, sporadic grains are observed at the surface often accompanied by small internal twins.
- While a central twin is present, there is evidence of grains with a low angle of misorientation on either side, with misorientations with respect to the matrix being less than 15° .

Since the plastic strain is related to the dislocation density, following an approach adopted elsewhere,^[26] the geometrically necessary dislocation density (GND), determined from the lattice curvature within the crystals, is plotted in Figure 7(c), while Figure 7(a) and (b) represents the kernel angle misorientation (KAM) of surface grains and the surrounding microstructure.

The main features are the two high-angled grain regions formed in the center which appear to be annealing twins presenting a misorientation of $\sim 60^\circ$. Surrounding the twins is a subgrain structure comprising of several attached low-angled grain boundaries ranging from (7° to 12°) misorientation with respect to the single-crystal matrix. Several dislocation dense boundaries are seen within Figure 7(a) focused on the

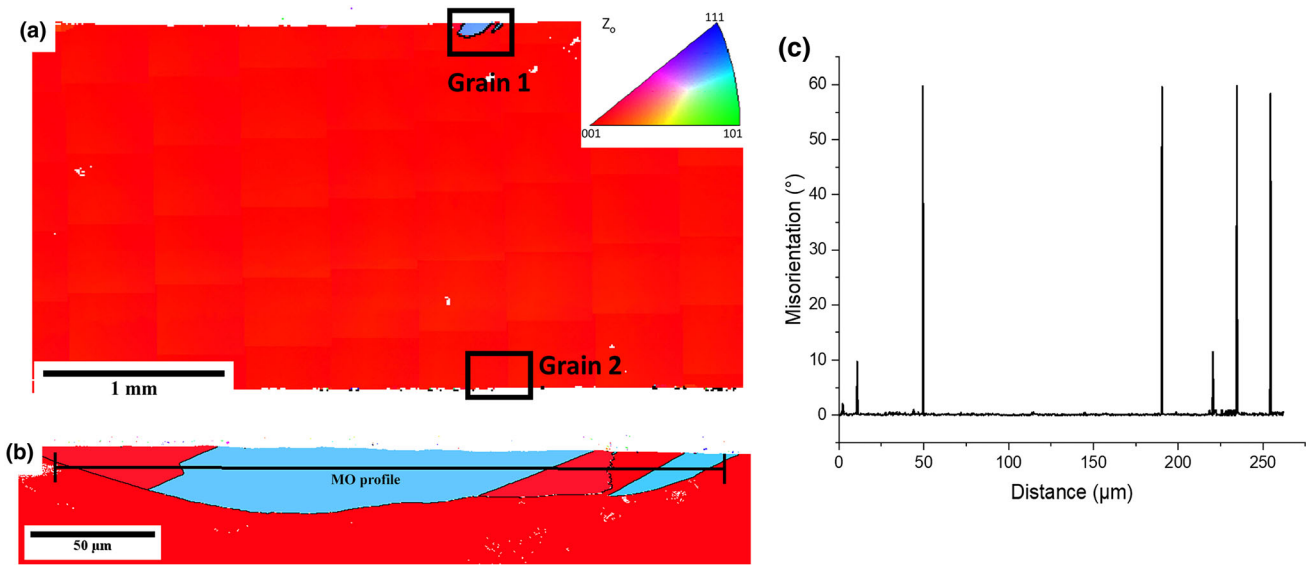


Fig. 6—Microstructure after isothermal hold for sample S1 showing the formation of surface-recrystallized grains and subgrains: (a) Inverse pole figure (IPF-Z)-derived orientation map (OIM) with Z describing the direction transverse to the direction of solidification, (b) higher resolution map focusing on the surface grains, and (c) a line plot of the misorientation between successive measurement points, which traverses the length of the surface.

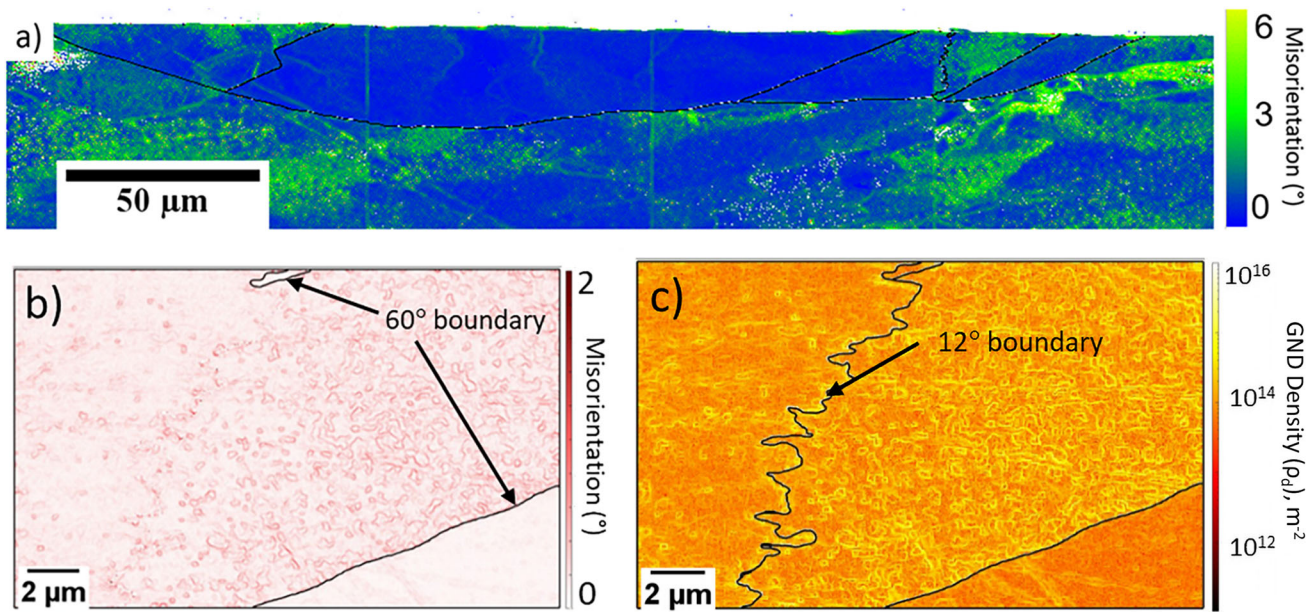


Fig. 7—Grain 1 from Fig. 6. Surface subgrain structure formed during isothermal holding of sample S1 (a) KAM map of the grains and surrounding area (b) KAM map of subgrain structure with 60° boundaries indicated (c) GND map of subgrain structure with 12° boundary between subgrains indicated.

periphery of the grain area and within $20\ \mu\text{m}$ of the specimen surface. In addition, the kernel angle misorientation (KAM) outside of the twin grains is substantially higher than that from within the boundary, with the high-angled grain presenting a relatively uniform orientation in comparison to the surrounding area.

Figure 8 shows another instance of a surface grain in sample S1 at a surface along the long edge, which is opposite to the long edge shown in Figure 7. The GND

maps reveals a dislocation density (ρ_d) difference between the 5° misorientated subgrain, $\rho_d = \sim 10^{14}\ \text{m}^{-2}$ within the subgrain, and the surrounding area, $\rho_d = \sim 10^{15}\ \text{m}^{-2}$. There is a significant number of low-angled subgrain boundaries (1° to 3°) in the adjacent areas ahead of this grain, as depicted by dislocation dense boundaries, $\rho_d = > 10^{15}\ \text{m}^{-2}$. The point to emphasize is the existence of a tenfold increase in GND ahead of the subgrain compared to within it.

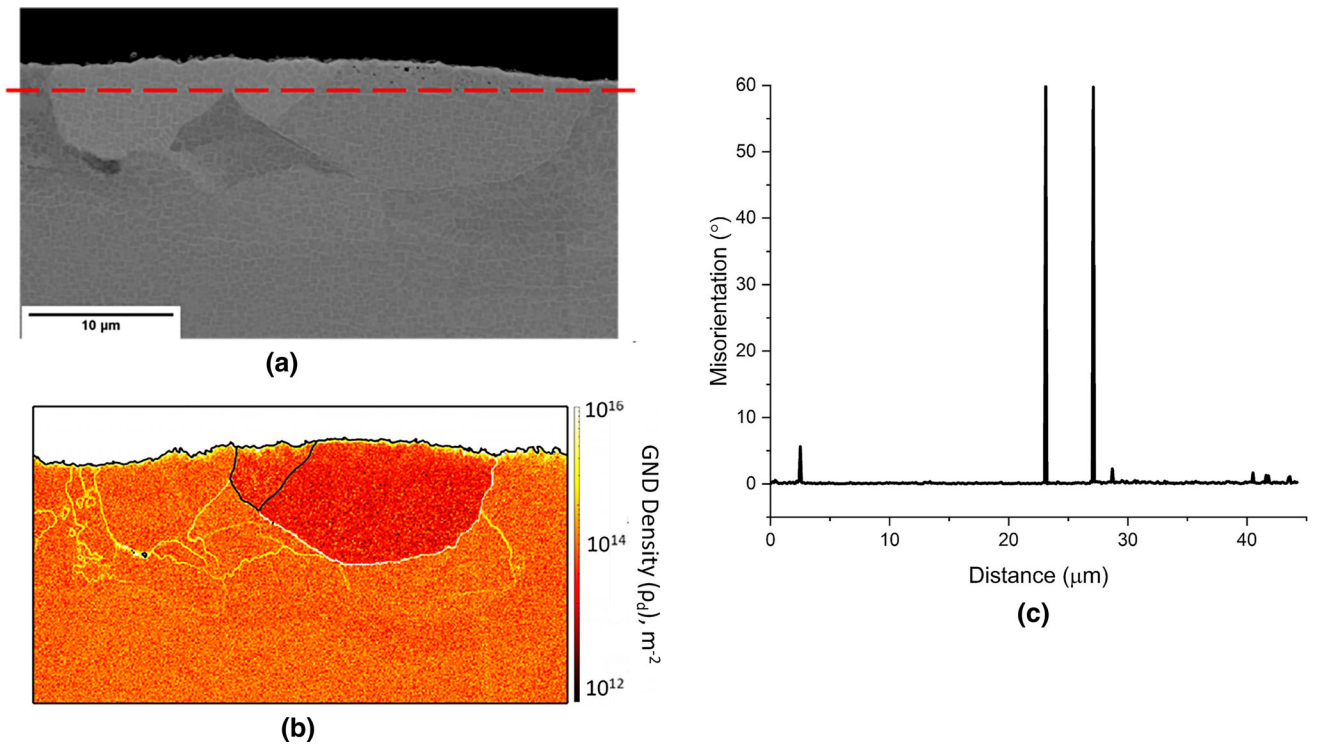


Fig. 8—*Grain 2* from Fig. 6. Surface subgrain structure formed during isothermal holding of sample S1 (a) backscattered electron image of the small surface grain in sample S1 (b) GND map of the subgrain structure with a 5° boundary between the subgrains indicated, and (c) misorientation profile across the sample [across dashed line shown in (a)].

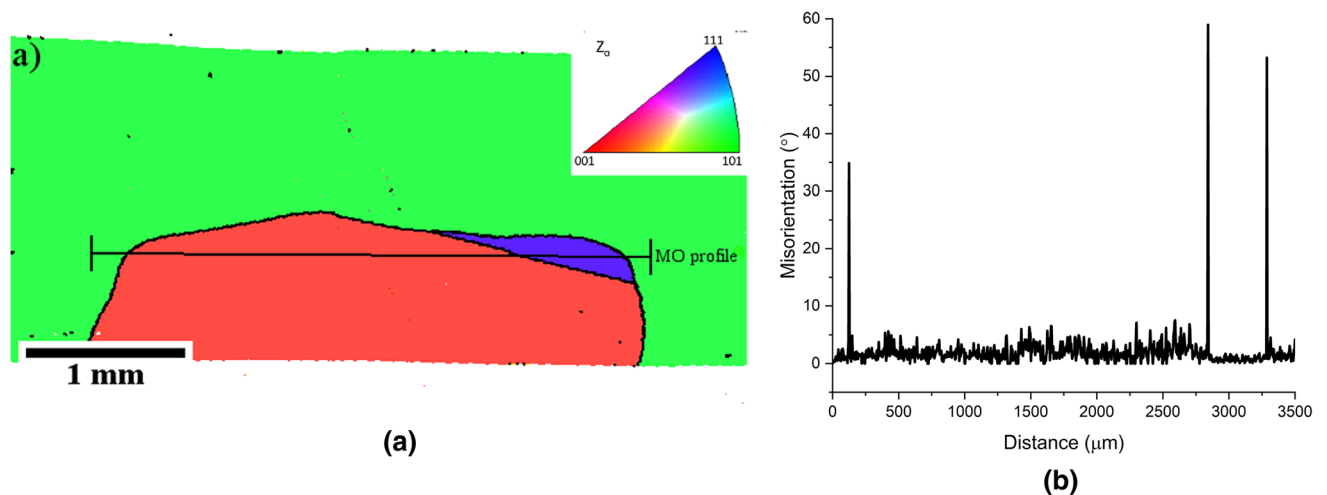


Fig. 9—Microstructure after isothermal hold for sample S2 showing the formation of a large, recrystallized grain (a) Inverse pole figure (IPF-Z) derived orientation map (OIM) of sample S2 with Z describing the direction transverse to the direction of solidification, (b) misorientation profile across the grain.

The gage length microstructure of sample S2 was also evaluated using EBSD to relate the resistance change to the evolution of the microstructure. An inverse pole figure (IPF-Z) with Z being the length of the specimen is shown in Figure 9, revealing that the gage length contains a single large high-angled grain which has consumed roughly half of the gage area. Figure 9(b) shows the misorientation between successive

measurement points [following the black line in Figure 9(a)] showing that the grain is misoriented $\sim 35^\circ$ in respect to the gage. The following observations can be made:

- (a) Unlike the as-cast sample S1, there is evidence of recrystallization occurring within the bulk material. Only one large grain is observed in the gage

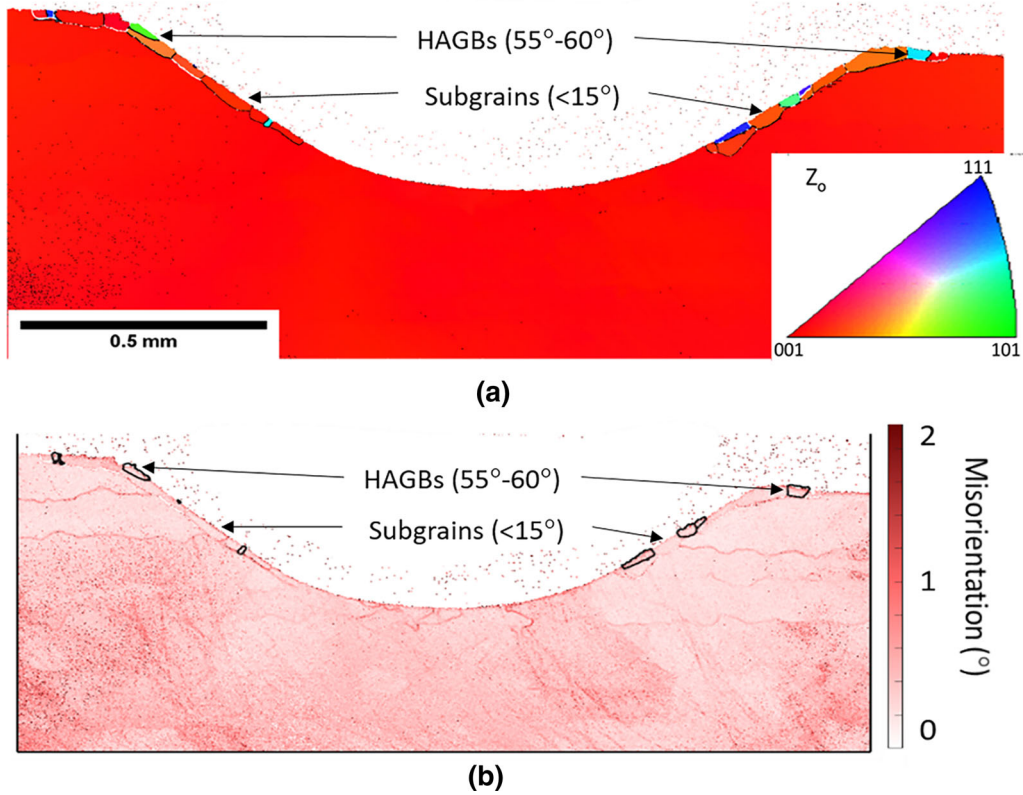


Fig. 10—Microstructure after isothermal hold for sample S3 showing the formation of surface-recrystallized grains and subgrains: (a) inverse pole figure (IPF-Z) derived orientation map (OIM) of sample S3 with Z describing the direction transverse to the direction of solidification, and (b) the corresponding KAM.

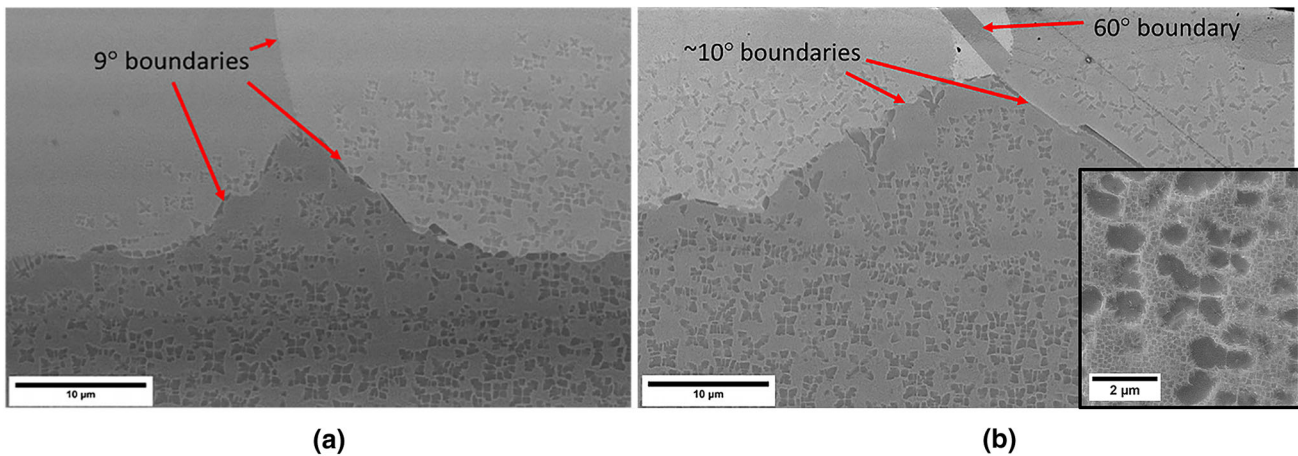


Fig. 11—Surface subgrain structure formed after displacement-controlled cooling of sample S3 (a) the right of the notch in Fig. 10 (b) the area left of the notch in Fig. 10, respectively. The inset depicts a higher magnification image of the butterfly morphology γ' .

length, in contrast to the isolated nature of those seen in the as-cast condition (sample S1).

- (b) A twin has formed within the recrystallized region, the same observation is seen within the small RX grains in sample S1.

The IPF map of sample S3 is shown in Figure 10(a), where the formation of several small subgrains on the surface, with misorientation ranging from (3° to 11°), is

observed. The size of these grains is typically $\sim 100 \mu\text{m}$ and many contain internal 60° twin boundaries. The KAM map shows significant subgrain formation across the substrate surface and detects misorientation boundaries associated with solutioned dendritic regions (depicted as coherent boundaries along the length of the specimen). High-angled boundaries are denoted in the KAM with black borders. These grains are exclusively

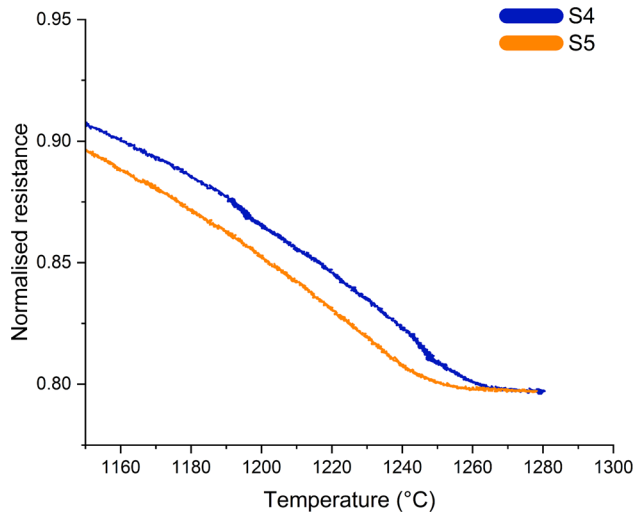


Fig. 12—Stage I: Plot of normalized resistance vs temperature during the 1st heating cycle under zero load for samples 4 and 5.

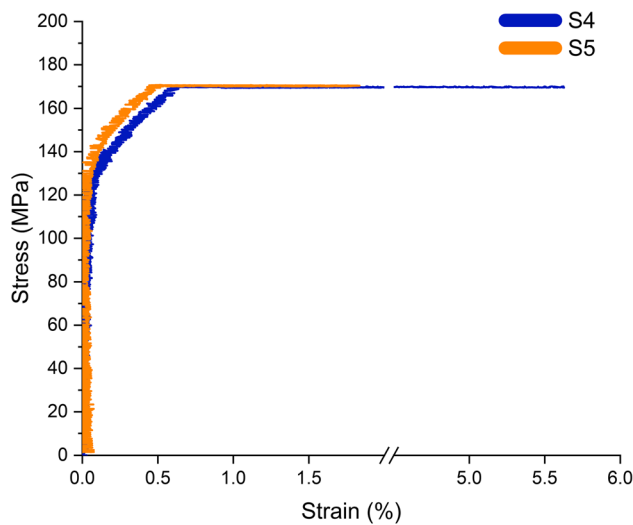


Fig. 13—Stage II: Evolution of stress and plastic strain during isothermal hold at 1150 °C showing the yield stress and plastic deformation in samples S4 and S5.

(55° to 60°) in misorientation with respect to the substrate and surrounding subgrains.

Backscattered images of the subgrain boundaries are shown in Figure 11. Given sample S3 is not annealed, a significant amount of the γ' precipitates possess a butterfly morphology, as reported in.^[28] This morphology is not limited to the substrate but is also prevalent throughout the subgrains. A butterfly precipitate morphology γ' is associated with a deformed microstructure, which is a combination of rafting and octa-dendritic growth.^[24] The deformed γ' precipitate morphology is prominent around the subgrain boundaries, and the number of deformed precipitates decreases significantly towards the edge of the specimen [*i.e.*, to the left of Figure 11(a)].

B. Evolution of Resistance and Microstructure Following Isothermal Loading and Isothermal Hold

Figure 12 is a plot of the normalized resistance following^[17] with temperature during the 1st heating cycle under zero load for samples S4 and S5. The γ' solvus temperature is indicated by the plateau shown by the normalized resistance approaching ~1260 °C. A difference in local solvus temperature of ~10 °C is observed in the two cases, where the sample with the lower normalized resistance has a lower local solvus. Similar observations have been reported in.^[17]

In the proceeding section, the evolution of the microstructure after solutioning following an accumulation of plastic strain during displacement-controlled cooling was considered. The resistance, in addition to being dictated by recovery, is also affected by dissolution of the eutectic. Thus, pre-solutioned specimens without eutectic (samples S4 and S5) are considered, where the absence of eutectic precludes the contribution of the latter effect. Further, to additionally delineate the history dependence of deformation on the evolution of stress and plastic strain, tensile deformation was induced at 1150 °C at the end of the 1st cooling cycle (sample cooled under zero load from 1300 to 1150 °C), instead of being accumulated during displacement-controlled cooling, as in samples S1 and S2. Figure 13 presents the evolution of stress with plastic strain for samples S4 and S5, which were loaded at a rate of 2 N s⁻¹ up to ~170 MPa and then allowed to creep at constant load at 1150 °C. In both cases, a yield stress of ~125 MPa can be deduced, and typically beyond ~0.5 pct plastic strain, creep prevails. Two levels of plastic strain were considered, *i.e.*, ~1.8 pct (sample S4) and 5.6 pct (sample S5).

The variation in resistance on subsequent heating to 1280 °C and during the isothermal hold is plotted in Figure 14 for samples S4 and S5, respectively. Figure 15(a) and (b) is the orientation image maps (OIM) that show the evolution of the RX grains within the gage. The following observations can be made:

- There is a decrease in normalized resistance of $\sim 2 \times 10^{-2}$ in sample S4, but a significantly smaller decrease of $\sim 2 \times 10^{-3}$ in sample S5.
- There are also broadly 3 regimes in the temporal evolution of resistance. However, unlike in the starting as-cast condition, the initial decrease is rapid compared with a gradual decrease thereafter.
- There is a marked difference in the extent of RX. In case of sample S5, complete RX is observed within the gage region, with grains of random orientation, while this is not observed in sample S4. Rather, an isolated subgrain with misorientation of ~12° with the primary grain is observed.
- Another marked difference is observed between the two cases of loading, *i.e.*, accumulated plastic strain (samples S1 and S2) and evolving stress under displacement-controlled cooling and that applied at a single temperature (sample S5)—for a comparable stress and plastic strain and decrease in resistance, there is a remarkable difference in

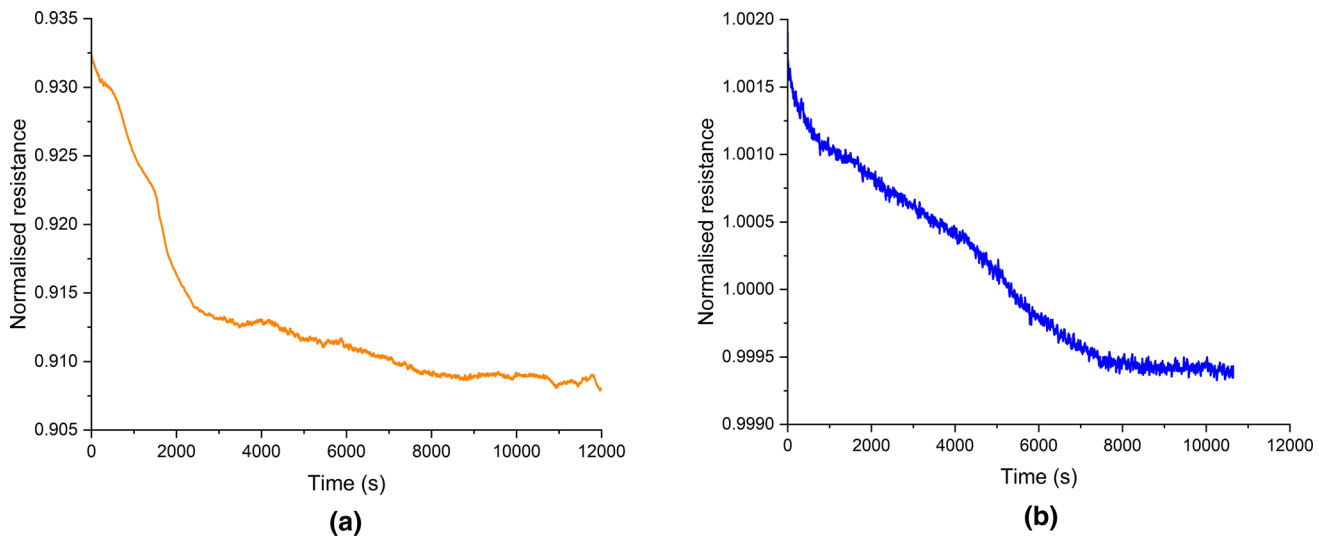


Fig. 14—Stage III: Variation of normalized resistance indicating recovery in samples (a) S4 and (b) S5 during isothermal hold.

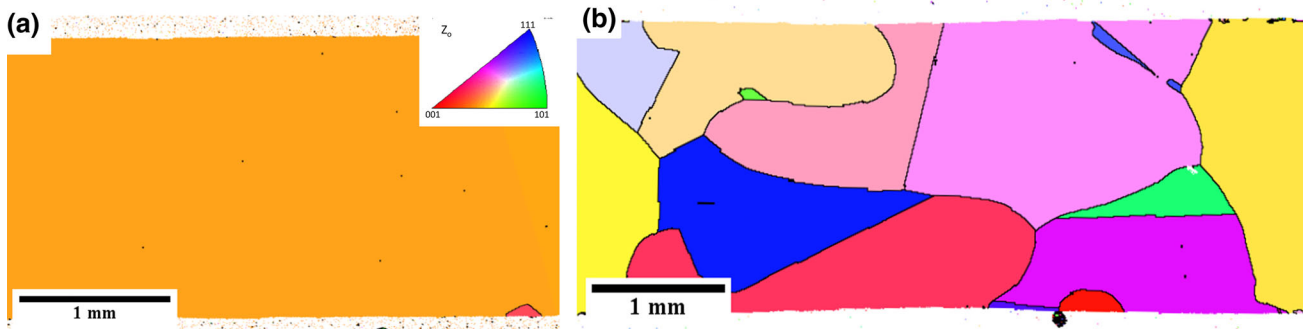


Fig. 15—Inverse pole figure (IPF-Z) derived orientation image maps (OIMs) for samples S4 and S5 following isothermal hold at 1280 °C: (a) sample S4 and (b) sample S5.

the amount of RX observed between the two cases.

The microstructure after annealing of sample S4 and sample S5 is shown in Figure 16. Both microstructures display a uniform cubic γ' morphology, consistent with observations from unstrained and solutioned specimens. No evidence of the butterfly morphology associated with deformation is seen here. The boundaries continue to show the “primary type” γ' morphology, albeit these precipitates are coherent with the γ -matrix within the gage length. Their occurrence is predisposed to the grain boundary.

IV. DISCUSSION

The plastic strain is obtained from Eq. [1], under the assumption that the intrinsic resistivity of the material is un-affected by the induced deformation, and the change in resistance is primarily governed by shape changes, *i.e.*, increasing L/A during tension and decreasing L/A during compression. During subsequent isothermal hold under zero load, any change in the measured resistance

must be, therefore, attributed only to the changing intrinsic resistivity. Resistance measurements throughout the study have been normalized using the room temperature resistance to provide more accurate comparison of changes in electrical properties between specimens.

First, the change in resistivity is dependent on the volume fraction of γ' within the gage region. Specifically, it has been observed that precipitate coarsening at sub-solvus temperatures leads to decreasing resistance, owing to a reduction in γ/γ' interfacial area resulting in reduced electron scattering at interfacial sites.^[18] A more potent case exists in the case of additively built microstructures, where precipitate sizes of the order of ~ 5 nm^[29] result in a markedly higher resistivity (~ 100 to 150 n Ω m) in the as-built condition, compared with the case where the re-precipitated γ' following heat treatment is characterized by a precipitate size of ~ 100 nm.^[30] However, this effect can be negated in the present experiments, since the isothermal hold is above the local solvus, as indicated by the normalized resistance curve, as in Figures 3 and 12. Another contribution to the resistance is through coarsening of the grain structure if a polycrystalline aggregate exists. Again, this is most

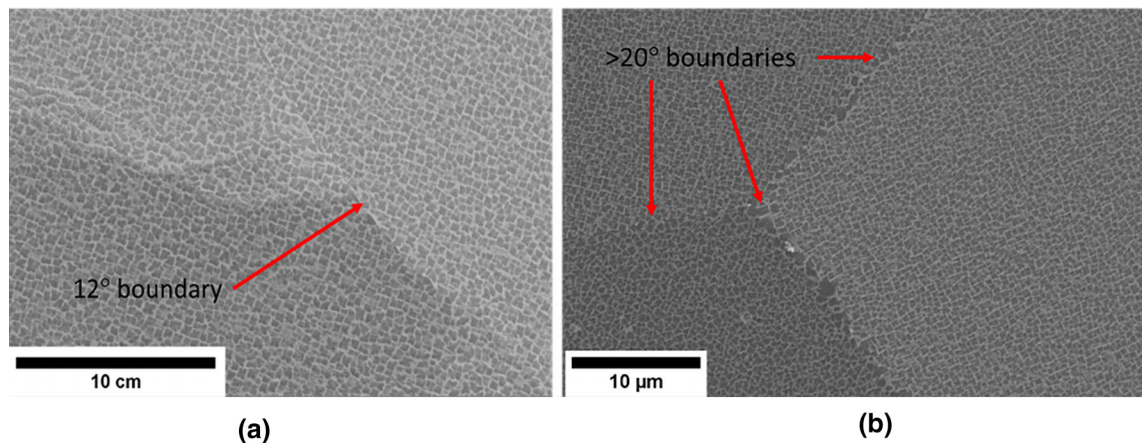


Fig. 16—Backscattered electron images showing (a) a uniform γ' precipitate morphology observed within sample S4 at subgrain boundaries (post-anneal) (b) Structure of γ' precipitates within sample S5 recrystallized grains post-anneal.

potent in case of very fine grain structures and thin films, where the grain size is of the order of the specimen thickness, and comparable to the mean-free path of the electrons.^[31] In the case of samples S1 and S4, this is certainly not the case, since the surface grains are sporadic, and the matrix is essentially single crystal. Further, when a fully recrystallized (RX) microstructure exists, as in sample S5, there is hardly any decrease in resistance and the grain size as in Figure 16 is of the order of mm.

Therefore, in lieu of the above arguments, it can be concluded that the decrease in normalised resistance of $\sim 2 \times 10^{-2}$ in case of samples S1 and S4 must arise during the recovery stages that precedes RX, as the dislocations re-arrange themselves into low energy configurations.^[21] In each case, the IPF maps from Figures 6(a) and 15(a) show that RX is extremely limited with only a few less than $150 \mu\text{m}$ size grains forming low angle misorientation with the matrix that are scattered sparingly across the surface. Another important aspect relates to the negligible decrease in resistance when RX dominates, as for sample S5 in Figure 14(a) from which it can be concluded that that the decrease in resistance (resistivity) only relates to recovery and that when recovery is negligible/absent, then only is RX dominant. This is further supported when sample S2 is considered. In sample S2, roughly half of the gage is consumed and the drop in normalized resistance $\sim 1 \times 10^{-2}$. The fact that complete RX occurs when recovery is incomplete is also observed in case of dynamic recrystallization (DRX), which is prominent at high strain rates and low temperatures.^[32] A prior approach was also adopted by Cox *et al.*^[4] to measure RX through a similar resistance-based approach, but in contrast to our results, they have reported an increase in resistance followed by a plateau during the isothermal hold period. This is contrary to what we report, but importantly the increasing trend exhibited by resistance in their study contradicts not only the nature of recovery, but also that RX is accompanied by a negligible change in resistance, as in our study. Another point to note is that during the isothermal hold, there is a small increase in grip

displacement of $\sim 5 \mu\text{m}$. For a central gage length of $\sim (2.75 \text{ to } 3 \text{ mm})$, this is equivalent to a tensile strain rate of $\sim 10^{-7} \text{ s}^{-1}$. This primarily arises from the load cell sensitivity, which is $\pm 0.5 \text{ kN}$. However, this strain rate is significantly smaller than the strain rate during the displacement-controlled cooling, which is $\sim 10^{-4} \text{ s}^{-1}$. Hence, any additional deformation induced during the isothermal hold can be neglected.

A stark difference can be observed in the temporal evolution of resistance during the isothermal hold in case of samples S2 and S5 for comparable plastic strains of $\sim (4.8 \text{ to } 5.5 \text{ pct})$; Figures 4(b) and 13. The key difference is the loading path, which results in different stresses being experienced by each specimen. In case of sample S2, where the sample was cooled under displacement control, it is evident that the onset of hardening arising from precipitation occurs at $\sim 1225 \text{ }^\circ\text{C}$. Up to that stage, the plastic strain is $\sim 2 \text{ pct}$, which occurs through easy glide with minimal hardening. It is the hardening strain that leads to an increased dislocation density. This in turn is dictated by the local solvus temperature, as systematically analyzed in.^[17] No such easy glide exists in the case of sample S5, which results in a greater stress under which creep occurs, as revealed by a significantly high yield stress. This a very important point in terms of deriving maps (plastic strain vs isothermal hold time) for the propensity of RX, since it is the strain path that affects the hardening strain that develops. This corresponds to the looping of dislocations around the precipitates during the evolution of stress and plastic strain^[21] and clearly this impacts the extent of RX seen when comparing samples S2 and S5. In addition, there is stark differences in the number of RX grains observed in samples S2 and S5, Figures 9(a) and 15(b), respectively. In sample S2, a large unidirectional grain has formed in contrast to the polygranular structure seen in sample S5. This is presumed to be a result of multiple RX grain nucleation events arising in sample S5 and a lower propensity for the same RX nucleation events in sample S2. Although the specimens undergo similar strain accumulation, the strain path

plays a key role in the accumulation of dislocations and the propensity for RX.

The nucleation of RX is related to the development of subgrains.^[6] However, more recently it has been suggested that pre-existing grains present at the surface of a casting, such as surface eutectic, can act as potent nuclei for RX.^[11,28] In an earlier study, it was shown that such surface grains are formed during accumulated stress and plastic strain during prior displacement-controlled cooling akin to directional solidification. Moreover, it was also observed that the propensity for formation of these grains was related to the normalized resistance. Higher normalized resistance is associated with a higher local solvus temperature; thus, a higher γ' precipitation temperature is observed leading to an earlier onset of hardening. Specimens with higher normalized resistance were shown to have an increased spatial occurrence of these surface grains resulting from greater hardening strain accumulation during displacement-controlled cooling.^[28] These grains are also consistently observed in sample S3, but importantly, there exists a bi-modal precipitate morphology. γ' precipitates formed within the gage volume shows the butterfly morphology, which is a combination of rafting and octo-dendritic growth along the cube edges,^[26] which must be delineated from the fine size γ' precipitates that nucleates and grows during quench at 1215 °C. There are two important facts:

- γ' phase precipitates with a butterfly morphology also exist in the surface grains, and it is evident that these surface grains have formed close to the solvus.
- The majority of these grains have low angle boundaries with respect to the substrate; hence, they are subgrains.

The mechanism for the formation of these grains is key, but is not considered within the scope of this study. In the case of the subgrains, the growth of these grains must occur through absorption of dislocations. Continued absorption of dislocations results in a high-angle boundary with a high mobility which can then sweep through the strained matrix. There is a marked absence of the γ' butterfly morphology within the fully recrystallized microstructure (sample S5), instead a uniform cuboidal structure is seen throughout. This shows the presence of the butterfly morphology is only present within the strained matrix. The growth of RX occurs above the solvus during the isothermal hold where the deformed matrix is “restructured” as high-angle grain boundaries sweep through the matrix. Consequently, γ' precipitates nucleate and grow with a uniform cuboidal morphology within the strain-free γ matrix during subsequent cooling.

Strain-induced boundary migration (SIBM) is a key mechanism by which recrystallization consumes deformed material.^[33,34] SIBM is the migration of grain boundaries across deformed material, leaving a deformation-free material in the wake of the progressing boundary. The mechanism requires a significant dislocation gradient to be present between neighboring grains, from which the least deformed grain will

gradually consume the neighbor. Rudiments of SIBM can be seen clearly in Figure 7(c) where a deformed subgrain is being consumed owing to a dislocation density difference $\sim 10^2 \text{ m}^{-2}$. High dislocation density loops observed in the deformed grain are on the scale of γ' precipitates, $\sim 50 \mu\text{m}$, suggesting they are interfacial dislocations. The observation of boundary bulging confirms that SIBM plays an active role in the recrystallization mechanism of Ni-based superalloys. Interestingly, the moment captured involves the movement of a subgrain boundary ($< 15^\circ$) and confirms the existence of deformed subgrains in the material post-annealing. It is unclear whether the deformation-free subgrain with the active boundary was present prior to annealing or whether this formed during annealing. However, this does indicate that deformed subgrains undergo further recovery through alternative mechanisms during annealing. This may provide evidence for secondary subgrain nucleation events occurring separate from those manifesting after cooling. Further observations should be made in future studies.

In summary, the temporal variation in resistance during an isothermal hold is related to the extent of recovery. When recovery is close to completion, as in sample S4, a plateau is observed in the resistance curve, which is dictated by variation in resistivity (L/A is constant, as in Eq. [1]). When RX prevails, then recovery is incomplete, as in the case of sample S5. The rate of recovery when RX is incomplete is also affected by other factors, which is mainly dependent on the pedigree of the initial microstructure. This is mainly biased in case of the as-cast condition since the decrease in resistance (or resistivity) is also dependent on the dissolution kinetics of γ' precipitates. Not only is there the presence of eutectic, but also a range in composition across the dendrite cross section owing to the presence of microsegregation, which results in a range of solvus temperature.^[17] The local solvus temperature is highest at the dendrite lobe periphery and lowest at the dendrite core.^[35] Therefore, dissolution of eutectic and simultaneous homogenization leads to a decrease in the γ' volume fraction, both within the inter-dendritic region, as well as within the dendrite morphology, resulting in a resistance decrease. This aspect is interesting and merits further study to obtain further information on how these factors influence the mechanical behavior in the as-cast state. Although some efforts have been made using the banding to compare specimens,^[17] there is significant opportunity for these to be further explored. In particular, the variation in the response of the as-cast material to the methodology presented in this work would provide significant insight into the influence of the eutectic/ γ' on static recrystallization. However, there have been several difficulties highlighted in this study regarding the reliability of the as-cast material. A study of the as-cast eutectic behavior and solutioning effects would require a far greater number of specimens than was used in these trials but presents an interesting avenue for further work. However, for a more accurate assessment of the kinetics of recovery, it is imperative to minimize these other effects; this justifies the choice of a solutioned microstructure as the starting condition.

This study has confirmed the findings of several prior authors but raises further questions regarding RX in single-crystal Ni-base superalloys. The formation of subgrains prior to an isothermal hold is evident, but the observation that these subgrains are deformed leads to further questions regarding their exact contributions to RX during post-cast heat treatments. This requires further study using an interrupted test regime to determine the exact temperature range associated with their formation and further to this, what happens to these during heat treatment. This will be particularly interesting when the material is in the as-cast state, where local composition will also play a key role in their formation and strain accumulation. In addition, the formation of such grains should be further related to geometric discontinuities within material. The plastic strain accumulated from thermal contraction should be greater investigated in relation to these geometric features to further apply these findings to turbine blade design.

V. CONCLUSIONS

In this study, samples of the single-crystal nickel base superalloy, CMSX-4, were subjected to thermal–mechanical conditions, and an electrothermal mechanical testing (ETMT) system was used to replicate the conditions existing during casting and subsequent solution heat treatment. The influence of thermo-mechanical behavior and microstructure on recovery and recrystallization in single-crystal superalloys has been identified. The study found the following:

- (1) Recrystallization occurs in Ni-base superalloys only when recovery is incomplete and is dependent on both the history of the strain path and the magnitude of accumulated strain. Complete recrystallization is only evident in isothermally strained samples. Complete recrystallization is not replicated for displacement-control cooling with the same strain accumulation, indicating the temperature at which plasticity is accumulated is a key factor.
- (2) Strained subgrains and deformation twins occur at the sample surface following displacement-controlled cooling in solution heat-treated alloys. γ' precipitates with a butterfly morphology are always observed in highly strained regions.
- (3) The migration of recrystallized grain boundaries is consistent with the elimination of lattice curvature associated with the density of geometrically necessary dislocations. The migration of subgrains, however, can occur only after they are transformed to high-angle grain boundaries.
- (4) When measuring recovery through resistivity changes, the most accurate data are obtained when strains are low. For high strains, resistivity is dominated by the sample geometry changes, making measurements less reliable.
- (5) Recovery is shown to be traceable in resistance measurements when recrystallization is less well

defined. Homogenized samples provide the most reliable results, while the interpretations are more limited when compositional inhomogeneity exists in as-cast structures.

ACKNOWLEDGMENTS

Samuel Perry wishes to acknowledge EPSRC CDT (Grant No: EP/S515486/1) in Innovative Metal Processing for providing the PhD studentship for this study and Rolls-Royce Plc for providing the CMSX-4® used for testing.

CONFLICT OF INTEREST

On behalf of all authors, the corresponding author states that there is no conflict of interest.

OPEN ACCESS

This article is licensed under a Creative Commons Attribution 4.0 International License, which permits use, sharing, adaptation, distribution and reproduction in any medium or format, as long as you give appropriate credit to the original author(s) and the source, provide a link to the Creative Commons licence, and indicate if changes were made. The images or other third party material in this article are included in the article's Creative Commons licence, unless indicated otherwise in a credit line to the material. If material is not included in the article's Creative Commons licence and your intended use is not permitted by statutory regulation or exceeds the permitted use, you will need to obtain permission directly from the copyright holder. To view a copy of this licence, visit <http://creativecommons.org/licenses/by/4.0/>.

REFERENCES

1. R.C. Reed: *The Superalloys: Fundamentals and Applications*, Cambridge University Press, Cambridge, 2006.
2. B. Hutchinson: *Scr. Metall. Mater.*, 1992, vol. 27, pp. 1471-75.
3. C. Panwisawas, H. Mathur, J.-C. Gebelin, D. Putman, C.M.F. Rae, and R.C. Reed: *Acta Mater.*, 2013, vol. 61, pp. 51-66.
4. D.C. Cox, B. Roebuck, C.M.F. Rae, and R.C. Reed: *Mater. Sci. Technol.*, 2013, vol. 19, pp. 440-46.
5. F.J. Humphreys and M. Hatherly: *Recrystallization and Related Annealing Phenomena*, 2nd ed. Elsevier, Oxford, 2004, pp. 169-213.
6. F.J. Humphreys and M. Hatherly: *Recrystallization and Related Annealing Phenomena*, 2nd ed. Elsevier, Oxford, 2004, pp. 215-IV.
7. J. Meng, T. Jin, X. Sun, and Z. Hu: *Mater. Sci. Eng. A*, 2010, vol. 527, pp. 6119-22.
8. A. Kreisler and R.D. Doherty: *Met. Sci.*, 1978, vol. 12, pp. 551-60.
9. R.K. Ray, W.B. Hutchinson, and B.J. Duggan: *Acta Metall.*, 1975, vol. 23, pp. 831-40.
10. H. Basoalto, S.K. Sondhi, B.F. Dyson, and M. McLean: *Superalloys 2004, Proc. Int. Symp., 10th*, 2004, pp. 897-906.
11. H.N. Mathur, C. Panwisawas, C.N. Jones, R.C. Reed, and C.M.F. Rae: *Acta Mater.*, 2017, vol. 129, pp. 112-23.

12. G. Brewster, H.B. Dong, N.R. Green, and N. D'Souza: *Metall. Mater. Trans. B*, 2008, vol. 39, pp. 87-93.
13. M. Long, N. Leriche, N.T. Niane, C. Labergere, H. Badreddine, and D. Grange: *J. Mater. Process. Technol.*, 2022, vol. 306, p. 117624.
14. C. Panwisawas, J.C. Gebelin, and R.C. Reed: *Mater. Sci. Technol.*, 2013, vol. 29, pp. 843-53.
15. Z. Li, J. Xiong, Q. Xu, J. Li, and B. Liu: *J. Mater. Process. Technol.*, 2015, vol. 217, pp. 1-2.
16. Y. Li, W. Xuan, J. Yang, Y. Zhou, G. Song, X. Ren, and Z. Ren: *China Foundry*, 2022, vol. 19, pp. 27-34.
17. N. D'Souza, B. Roebuck, D.M. Collins, G.D. West, and C. Panwisawas: *Mater. Sci. Eng. A*, 2020, vol. 773, p. 138862.
18. N. D'Souza, M.C. Hardy, B. Roebuck, W. Li, G.D. West, and D.M. Collins: *Metall. Mater. Trans. A*, 2022, vol. 53, pp. 2480-95.
19. B. Roebuck, D. Cox, and R. Reed: *Scr. Mater.*, 2001, vol. 44, pp. 917-21.
20. S. Sulzer, E. Alabort, A. Németh, B. Roebuck, and R. Reed: *Metall. Mater. Trans. A*, 2018, vol. 49, pp. 4214-235.
21. Y. Tang, M. Huang, J. Xiong, J. Li, and J. Zhu: *Acta Mater.*, 2017, vol. 126, pp. 336-45.
22. A. Cruzado, J. Llorca, and J. Segurado: *Int. J. Solids Struct.*, 2017, vol. 122-123, pp. 148-61.
23. S. Keshavarzand and S. Ghosh: *Acta Mater.*, 2013, vol. 61(17), pp. 6549-61.
24. H.G. Van Bueren: *Acta Metall.*, 1955, vol. 3, pp. 519-24.
25. R. Hielscher and H. Schaeben: *J. Appl. Crystallogr.*, 2008, vol. 41, pp. 1024-37.
26. W. Pantleon: *Scr. Mater.*, 2008, vol. 58, pp. 994-97.
27. E. Nembach, J. Pesicka, and E. Langmaack: *Mater. Sci. Eng. A*, 2003, vol. 362, pp. 264-73.
28. Y.T. Tang, N. D'Souza, B. Roebuck, P. Karamched, C. Panwisawas, and D.M. Collins: *Acta Mater.*, 2021, vol. 203, p. 116468.
29. V.D. Divya, R. Muñoz-Moreno, O.M.D.M. Messé, J.S. Barnard, S. Baker, T. Illston, and H.J. Stone: *Mater. Charact.*, 2016, vol. 114, pp. 62-74.
30. N. D'Souza, Rolls-Royce plc., unpublished research, 2022.
31. L. Tian, I. Anderson, T. Riedemann, and A. Russell: *Acta Mater.*, 2014, vol. 77, pp. 151-61.
32. A. Nicolay, G. Fiorucci, J.M. Franchet, J. Cormier, and N. Bozolo: *Acta Mater.*, 2019, vol. 174, pp. 406-17.
33. A. Paggi, G. Angella, and R. Donnini: *Mater. Charact.*, 2015, vol. 107, pp. 174-81.
34. P.A. Beck and P.R. Sperry: *J. Appl. Phys.*, 1950, vol. 21, pp. 150-52.
35. H.T. Pang, N. D'Souza, H. Dong, H.J. Stone, and C.M.F. Rae: *Metall. Mater. Trans. A*, 2015, vol. 47, pp. 889-906.

Publisher's Note Springer Nature remains neutral with regard to jurisdictional claims in published maps and institutional affiliations.